# Structure and kinetics of three-dimensional defects on the 10 1 -2 twin boundary in magnesium: Atomistic and phase-field simulations

Douglas Spearot, Vincent Taupin, Khanh Dang, Laurent Capolungo

# Structure and Kinetics of Three-Dimensional Defects on the $\{10\bar{1}2\}$ Twin Boundary in Magnesium: Atomistic and Phase-field Simulations

Douglas E. Spearot,[1,*] Vincent Taupin,[2] Khanh Dang,[1] and Laurent Capolungo[3]

[1] Department of Mechanical and Aerospace Engineering,
University of Florida, Gainesville, FL 32611, USA
*Corresponding author: dspearot@ufl.edu, 352-392-6747

[2] Université de Lorraine, CNRS, Arts et Métiers ParisTech, LEM3, F-57000 Metz, France

[3] Materials Science and Technology Division (MST-8), Los Alamos National Laboratory,
Los Alamos, NM 87545, USA

## Abstract

Twinning is an important plastic deformation mechanism in Mg. While computational and experimental efforts have studied the two-dimensional equilibrium structure of boundaries and facets that surround twin domains, little consideration has been given to three-dimensional nonequilibrium structures. Furthermore, the relationship between the structure of nonequilibrium facets and the kinetics of twinning is also not well understood. Thus, the objective of this work is to characterize the structure of three-dimensional defects on the $\{10\bar{1}2\}$ twin boundary and to study the kinetics associated with motion of the facets that bound these three-dimensional defects. Atomistic simulations show that the three-dimensional defects are bounded by nonequilibrium facets with prismatic/basal and twist pyramidal/pyramidal interfaces. The three-dimensional defects are surrounded on the $\{10\bar{1}2\}$ twin boundary by disconnection loops. The kinetics of the twin domain facets at finite temperature are analyzed by both molecular dynamics and a newly proposed anisotropic phase-field model. The latter allows the deconvolution of the competing role of interface energy, mobility and internal stress state. Molecular dynamics simulations show that inclined facets control the annihilation process; this behavior is captured in the phase-field model using mobility for the coherent twin boundary that is significantly lower than that of crater inclined facets. Further, molecular dynamics simulation results are best matched via the introduction of facet orientation dependent excess energies.

**Keywords:** Magnesium; Twinning; Dislocations; Disconnections; Atomistic Simulations; Phase-Field Modeling

## 1. Introduction

Twinning is a key deformation mechanism in Mg due to the low crystal symmetry of the hexagonal close packed (HCP) lattice (cf. (Barrett and El Kadiri, 2014a, 2014b; Kumar et al., 2018; Lentz et al., 2016; Wang et al., 2009a)). In particular, the $\{10\bar{1}2\}$ twin accommodates deformation along the c axis of the HCP crystal (Christian and Mahajan, 1995). Many atomistic simulation studies (Hagege et al., 1990; Morris et al., 2005; Pei et al., 2018, 2017; Wang et al., 2010) have focused on the structure of the $\{10\bar{1}2\}$ coherent twin boundary, which accounts for two parallel sides of a $\{10\bar{1}2\}$ twin domain. For example, Hagege et al. (Hagege et al., 1990) first reported two stable structures: (i) a mirror-symmetric structure often referred to as the "reflection" twin boundary and (ii) a microfaceted structure often referred to as the "glide" twin boundary because it includes a $< 10\bar{1}1 >$ relative translation. Using ab initio calculations with a large supercell, Wang et al. (Wang et al., 2010) reported that the reflection twin boundary has a slightly lower energy (by 1.9 mJ/m$^2$) than the glide twin boundary. This was confirmed by Pei et al. (Pei et al., 2018, 2017) using ab initio calculations, reporting an energy difference of approximately 2 mJ/m$^2$. Pei et al. also computed the phonon spectra of both twin boundary variants to show that the microfaceted twin is structurally unstable. Their results explain why twin boundaries with this structure are not observed experimentally in Mg even though their energies are very close to that of reflection twins.

Inherently, twins are three-dimensional domains bounded by different facets (Barrett and El Kadiri, 2014a, 2014b; Leclercq et al., 2014; Liu et al., 2014, 2016; Ostapovets and Gröger, 2014; Ostapovets and Serra, 2014; Wang et al., 2014, 2013; Xu et al., 2013; Zu et al., 2017), each with unique structure, admissible defects, energy and mobility. Overall, the correlation/coupling

between these properties controls the kinetics of twin growth. For example, one simple mechanism for thickening of twins perpendicular to the $\{10\bar{1}2\}$ boundaries is the nucleation and glide of $< 10\bar{1}1 >$ twinning dislocations along the $\{10\bar{1}2\}$ twin plane (cf. (Hirth et al., 2016; Spearot et al., 2019)). This increases the thickness of the twinned region by two atomic layers, which corresponds to the step height of the twinning dislocation. Indeed, $< 10\bar{1}1 >$ twinning dislocations belong to the class of line defects known as disconnections (Hirth et al., 2006).

In addition, growth of a twin domain requires migration or evolution of other interfaces. In the $< 10\bar{1}1 >$ direction, the twinned region is bound by the semicoherent prismatic/basal (PB) interface and usually the conjugate reflection twin (Wang et al., 2013; Xu et al., 2013). The migration of the PB interface was found (Ostapovets and Gröger, 2014; Ostapovets and Serra, 2014) to be associated with disconnection nucleation and motion. Disconnections can be nucleated at disclination dipoles, which exist at the intersection of the twin facets (Ostapovets and Serra, 2014), and may glide between the $\{10\bar{1}2\}$ boundary and the PB boundary under certain conditions (Barrett and El Kadiri, 2014a). Disconnections within the PB interface also accommodate the 3.72° misalignment of the basal and prismatic planes (Ostapovets and Serra, 2014). The boundaries perpendicular to the $< 10\bar{1}1 >$ direction in a three-dimensional twin ellipsoid were examined by Liu et al. (Liu et al., 2016) using high-resolution transmission electron microscopy (HRTEM). They reported that this boundary consists of facets of semicoherent prismatic/prismatic interfaces with a twist misorientation.

The two-dimensional equilibrium structure of each of the facets discussed above has been thoroughly analyzed. However, analogous to grain boundaries, nonequilibrium structures of

these interfaces will exist and this aspect of twin domain structure has not been previously explored. Furthermore, the relationship between the structure of twin domain facets and their kinetics is also not well understood. Thus, the objective of this work is to characterize the structure of three-dimensional defects on the $\{10\bar{1}2\}$ twin boundary and to study the kinetics associated with the motion of the facets that bound these three-dimensional defects.

Atomistic simulations are used to study the three-dimensional structure of defects created by the superposition of a dislocation shear loop onto the $\{10\bar{1}2\}$ twin boundary. Due to its geometry, this defect will be referred to as a "crater" for the remainder of this work. Atomistic simulations reveal that the three-dimensional defect is bounded on one side by the coherent twin boundary (CTB) and in orthogonal directions by nonequilibrium facets with prismatic/basal and twist pyramidal/pyramidal (PP1) interfaces. Further, molecular dynamics (MD) simulations of crater relaxation under its self-stress field show that the motion of the CTB, PB and PP1 interfaces are unique. To deconvolute the role of interface energy, mobility and driving force, a new anisotropic phase-field model is developed. This model allows the incorporation of interface type dependent energy and mobility, with the focus here limited to CTB, PB and PP1 interfaces. To reproduce the MD predictions, the phase-field model requires that the energy and mobility of nonequilibrium PB and PP1 interfaces must be higher than that of the coherent twin boundary. In addition, facet orientation dependent interface energies must be included.

## 2. Atomistic Simulation Geometry and $\{10\bar{1}2\}$ Twin Boundary Structure

All atomistic simulations in this work are performed using LAMMPS (Plimpton, 1995) with the modified embedded-atom method (MEAM) potential for Mg presented by Wu et al. (Wu et al.,

2015). This MEAM potential is a reparameterization of a prior MEAM potential by Kim et al. (Kim et al., 2009), providing a more accurate description of Mg lattice parameters, cohesive energy, and defect energies. Furthermore, since the MEAM potential accounts for angular dependence of atomic bonding, this potential is more appropriate for HCP Mg than earlier embedded-atom method (EAM) potentials by Sun et al. (Sun et al., 2006) or Liu et al. (Liu et al., 1996). For example, the EAM potential by Sun et al. provides an unrealistic stacking fault energy and predicts that the $\{10\bar{1}2\} < 10\bar{1}1 >$ twinning dislocation is unstable (Wu et al., 2015). Note, a recent EAM potential by Pei et al. (Pei et al., 2018) specifically includes twin boundary energies, stacking fault energies and some dislocation properties in the fitting database; this potential shows some promise as a non-angular dependent form for studying dislocation-twin interactions in Mg; select simulations are repeated using this potential for comparison with results generated using the Wu et al. MEAM potential.

Figure 1(a) shows the atomistic simulation geometry employed in this work. Two HCP Mg lattices are oriented such that opposing $\{10\bar{1}2\}$ planes lie parallel to the global XY plane. The X and Y dimensions of the simulation cell are chosen such that they are more than 4 times larger than the diameter of the dislocation loop superimposed onto the twin boundary. This ratio is determined through preliminary calculations considering convergence of the structure of the twin boundary defect. The Z dimension of the simulation cell is fixed as $L_Z = 23.60$ nm. In total, simulation models vary from 7.23 million atoms for a dislocation loop of 10 nm radius to 27.8 million atoms for a dislocation loop with 20 nm radius. Periodic boundary conditions are employed in all directions, resulting in a second twin boundary in the Z direction.

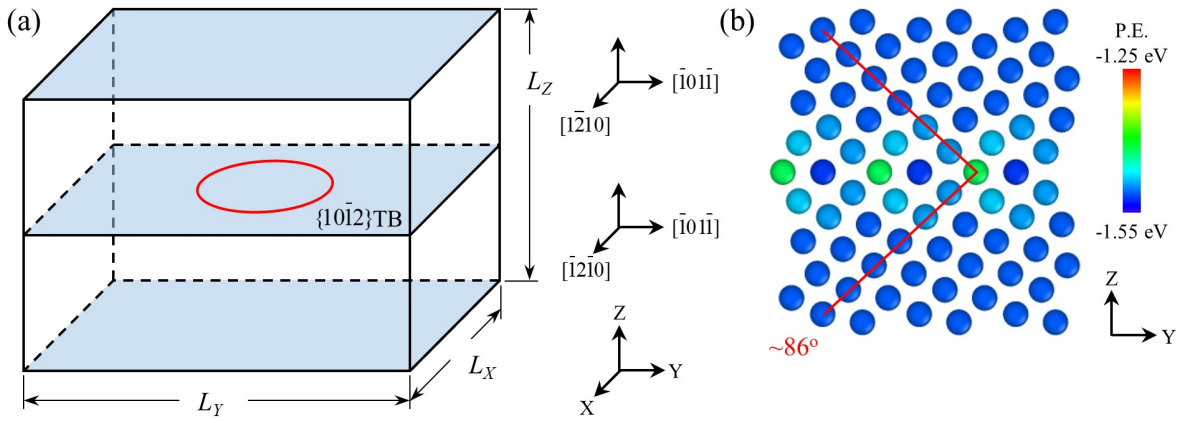


Figure 1. (a) Schematic of the $\{10\bar{1}2\}$ twin boundary simulation cell showing lattice orientations and the position of the superimposed dislocation loop (not drawn to scale). (b) $\{10\bar{1}2\}$ mirror twin boundary structure predicted using the MEAM potential by Wu et al. (Wu et al., 2015). Atoms are colored by atomic potential energy.

To determine the structure of the $\{10\bar{1}2\}$ twin boundary, a standard procedure (Rittner and Seidman, 1996; Spearot and McDowell, 2009) is employed whereby the opposing lattice regions are translated relative to each other to create different starting configurations for energy minimization calculations. Maximum translations in Y and Z directions are motivated by the Gibbs potential energy surface determined via density functional theory (DFT) calculations (Pei et al., 2017). At each starting configuration, three energy minimizations are performed using a nonlinear conjugate gradient method (Shewchuk, 1994), with the simulation cell boundaries allowed to expand or contact during the second minimization step to relax stresses within the simulation cell. Figure 1(b) shows the minimum energy structure of the $\{10\bar{1}2\}$ twin boundary identified by this approach. The boundary is atomically flat and mirror-symmetric with a misorientation of approximately 86.3° between basal planes in opposing lattice regions, in agreement with prior DFT and atomistic simulation results for the $\{10\bar{1}2\}$ reflection twin (Hagege et al., 1990; Morris et al., 2005; Pei et al., 2018, 2017; Wang et al., 2010). The excess energy of the coherent twin boundary is 0.142 J/m$^2$.

### 3. Construction of the Crater on the Twin Boundary

The displacement field of a dislocation shear loop is superimposed on the $\{10\bar{1}2\}$ twin boundary at the center of the simulation cell, as shown schematically in Fig. 1(a), using a modification of an approach first presented by Bitzek et al. (Bitzek et al., 2009) and used recently to study dislocation loops in Al (Dang et al., 2019, 2017). In this method, dislocation loops are constructed via superposition of the displacement field, $\boldsymbol{u}$, associated with N triangular dislocations. The displacement field of a single triangular dislocation was derived by Barnett (Barnett, 1985; Barnett and Balluffi, 2007),

$$\boldsymbol{u} = -\frac{\mathbf{b}\Omega}{4\pi} - \frac{1-2\nu}{8\pi(1-\nu)}[\boldsymbol{f}_{AB} + \boldsymbol{f}_{BC} + \boldsymbol{f}_{CA}] + \frac{1}{8\pi(1-\nu)}[\boldsymbol{g}_{AB} + \boldsymbol{g}_{BC} + \boldsymbol{g}_{CA}] \tag{1}$$

where,

$$\boldsymbol{f}_{AB} = (\mathbf{b}\wedge\mathbf{t}_{AB})\ln\left(\frac{R_B}{R_A}\cdot\frac{1+\boldsymbol{\lambda}_B\cdot\mathbf{t}_{AB}}{1+\boldsymbol{\lambda}_A\cdot\mathbf{t}_{AB}}\right) \tag{2}$$

and

$$\boldsymbol{g}_{AB} = \frac{[\mathbf{b}\cdot(\boldsymbol{\lambda}_A\wedge\boldsymbol{\lambda}_B)](\boldsymbol{\lambda}_A+\boldsymbol{\lambda}_B)}{1+\boldsymbol{\lambda}_A\cdot\boldsymbol{\lambda}_B} \quad . \tag{3}$$

Here, $\nu$ is Poisson's ratio and Ω is the solid angle that defines the volume between the point in space where the displacement is to be evaluated and the triangular dislocation *ABC*. The vector functions $\boldsymbol{f}_{AB}$ and $\boldsymbol{g}_{AB}$ depend on the Burgers vector of the dislocation, **b**, the unit tangent vectors that describe the triangle shape, **t**, and unit vectors, $\boldsymbol{\lambda}$, that describe the position of the general point in space relative to each triangle vertex (*A*, *B* and *C*). The scalars $R_A$ and $R_B$ are distances between the point of interest and the vertices A and B, respectively. Similar

expressions may be derived for the other $\boldsymbol{f}$ and $\boldsymbol{g}$ terms. Of course, Eqs. (1) – (3) do not describe the atom displacements close to the dislocation core; thus, energy minimization and brief thermal annealing, as described below, are performed after the insertion of the dislocation shear loop to resolve the structure of the resulting defect on the $\{10\bar{1}2\}$ twin boundary. For all simulations in this work, a Burgers vector magnitude $|\mathbf{b}| = 0.404$ nm is used, based on the generalized $\{10\bar{1}2\}$ planar fault curve calculated by Wang et al. (Wang et al., 2009b). All dislocation loops are created using a discretization of N = 16 triangles; supplemental simulations prove that the final structure of the twin boundary defect is consistent for larger values of N.

After superposition of the dislocation shear loop displacement field onto the $\{10\bar{1}2\}$ twin boundary, the structure of the resulting defect is resolved through a four-step process: (i) energy minimization via nonlinear conjugate gradient method, (ii) heating from 10 K to $0.4T_{melt} = 533$ K at a pressure of 0.0 bar over 10 ps, (iii) annealing at $0.4T_{melt}$ and a pressure of 0.0 bar for 10 ps, and (iv) energy minimization via nonlinear conjugate gradient method. Heating and annealing for a short period provides sufficient kinetic energy for the defect to find a lower energy structure after the second energy minimization step than found after the first energy minimization step.

**4. Structure of the Twin Boundary Defect**

For a dislocation loop radius of 15 nm, Figs. 2(a) and 2(b) show that a crater is created on the $\{10\bar{1}2\}$ twin boundary after the energy minimization and annealing procedure. Note, the simulation cell is much larger than the view provided in Fig. 2. The $\{10\bar{1}2\}$ twin boundary misorientation of approximately 86.3° is maintained both within and outside of the crater. The crater has prominent facets at its ends in the $< 10\bar{1}1 >$ directions, one of which is shown in Fig.

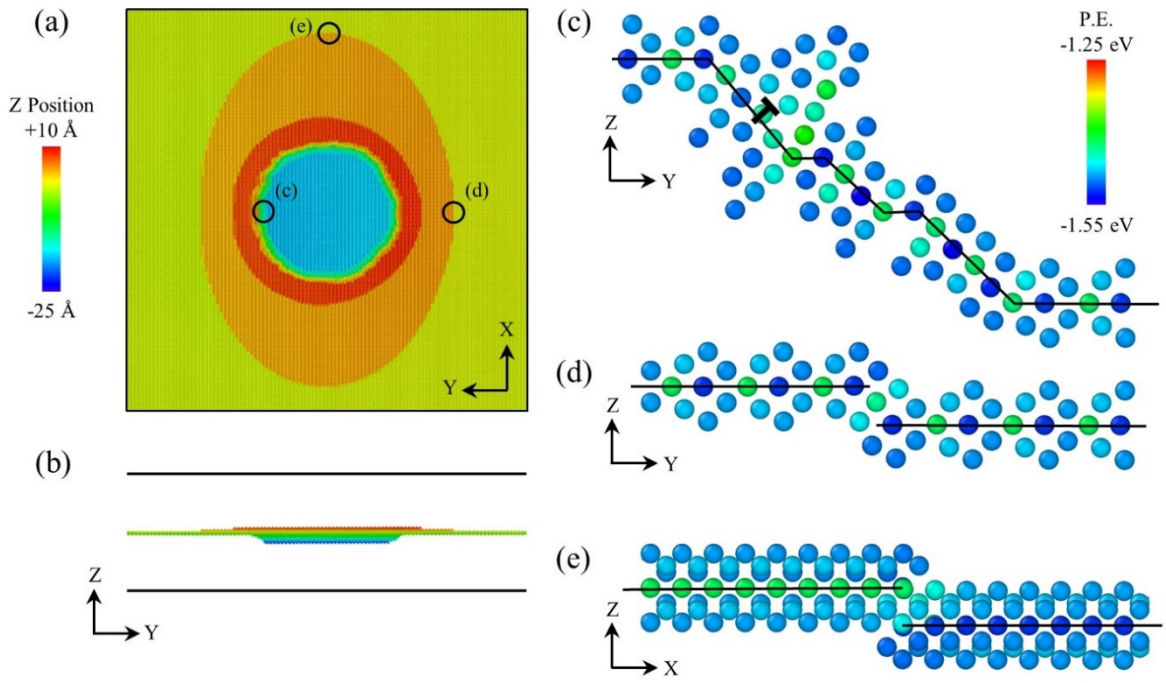


Figure 2. (a) Top and (b) side views of the 15 nm radius twin boundary crater after energy minimization (only a portion of the simulation cell is shown). Atoms are colored by their height in the Z direction, relative to the origin of the model. For X and Y lattice orientations refer to Fig. 1. Section views are provided of (c) the PB facet of the crater, showing misfit facet defects, (d) the disconnection ring in $< 10\bar{1}1 >$ and (e) the disconnection ring in $< 1\bar{2}10 >$ directions. Atoms are colored by atomic potential energy.

2(c). The crater has a total depth of 2.47 nm consisting of 25 $\{10\bar{1}2\}$ planes inclusive of the rim. The facet shown in Fig. 2(c) has a complex structure that includes facet jogs and the presence of an interfacial dislocation. In addition, two disconnection loops (Hirth and Pond, 1996; Kurtz et al., 1999) surround the crater. Figs. 2(d) and 2(e) show two-dimensional views of the outermost disconnection ring in the $< 10\bar{1}1 >$ and $< 1\bar{2}10 >$ directions. In Fig. 2(d), the disconnection consists of a vertical step with height 0.378 nm and a $< 10\bar{1}1 >$ dislocation with magnitude 0.0446 nm (based on analysis of the perfect dichromatic pattern (Kurtz et al., 1999)). Figure 2(e) shows that the disconnection is a perfect step in the $< 1\bar{2}10 >$ direction. The inner disconnection loop is nearly circular, but the outer disconnection loop is elliptical implying

differences in energies of the elastic strain field for edge and screw components of the disconnection loop. To confirm that the crater structure is independent of interatomic potential, the simulation procedure is repeated using the recent EAM potential of Pei et al. (Pei et al., 2018); a similar crater is obtained, with insignificant differences in the configuration of the outermost disconnection loop.

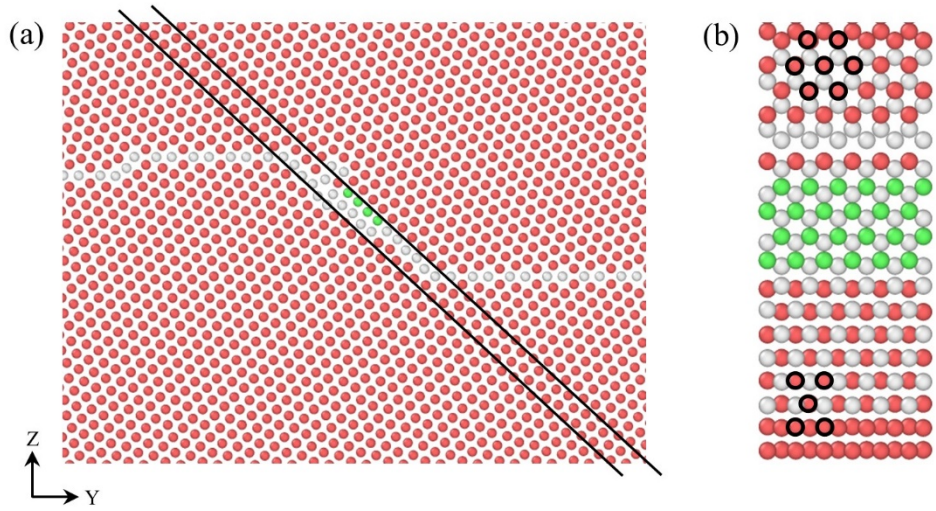


Figure 3. (a) Twin boundary island facet in the $[\bar{1}01\bar{1}]$ direction, which does not show a disconnection step but includes a dissociated dislocation within the interface. (b) Two dimensional slice of the facet identifying the prismatic/basal interface and the dissociation of a misfit dislocation. Atoms are colored by Common Neighbor Analysis.

Figures 3 and 4 provide a structural analysis of the facet interfaces on the $< 10\bar{1}1 >$ ends of the crater for a dislocation loop radius of 15 nm. On the left hand side of the island (Fig. 3(a) matching Fig. 2(c)), the facet interface contains a small discontinuity associated with an interfacial misfit dislocation. On the right side (Fig. 4(a)), a disconnection near the island floor and an interfacial dislocation within the interface are both present. The disconnection in Fig. 4(a) is identical to that which surrounds the basin, with step height of 0.378 nm and $< 10\bar{1}1 >$ dislocation with magnitude 0.0446 nm. Figures 3(b) and 4(b) show a two-dimensional slice through the facets at the orientations indicated in Figs. 3(a) and 4(a), respectively. The interfaces

are identified as prismatic/basal (PB) interfaces, in agreement with prior work on twin nucleation and motion in Mg (Leclercq et al., 2014; Wang et al., 2009b; Zu et al., 2017). The core spreading of the interfacial dislocation is also apparent. The observation of dissociated dislocations with different Burgers vectors and core spreading in each PB interface is attributed to the crystallography of the opposing lattice regions.

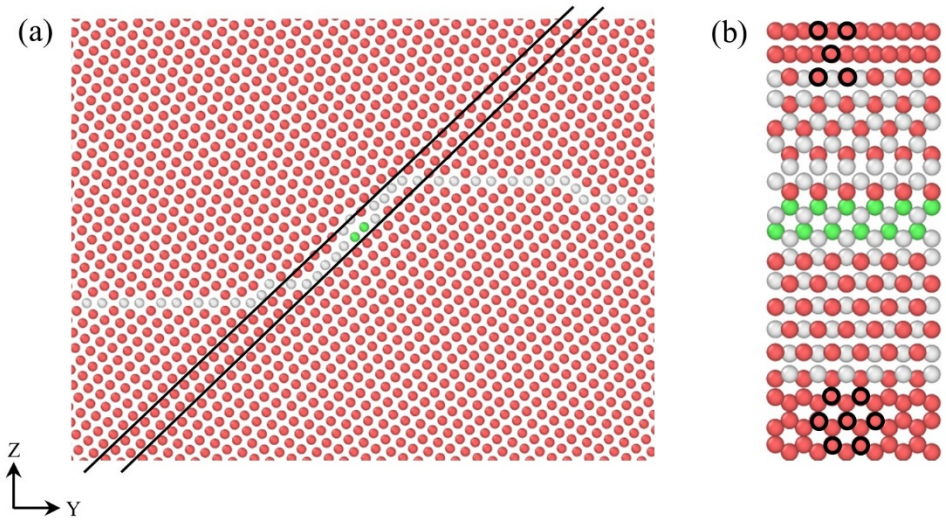


Figure 4. (a) Twin boundary island facet in the $[10\bar{1}1]$ direction, which shows a disconnection step near the bottom of the island and smaller steps associated with a dislocation within the interface. (b) Two dimensional slice of the facet identifying the prismatic/basal interface. Atoms are colored by Common Neighbor Analysis.

Figure 5 shows a two-dimensional slice through the crater in the X-Z plane. A disconnection step appears near the island floor with pure step height of 0.378 nm, identical to the disconnection loop that surrounds the island shown in Fig. 2(d). The interface between the opposing lattice regions is identified as a pyramidal-pyramidal (PP1) interface with a twist misorientation of approximately 77°. Note that the interface on the opposite side of the basin is symmetric to the one shown in Fig. 5, including the disconnection step near the crater floor. This observation is

different from that made in Figs. 3 and 4 for the PB interfaces, which are unique depending on the end of the crater examined.

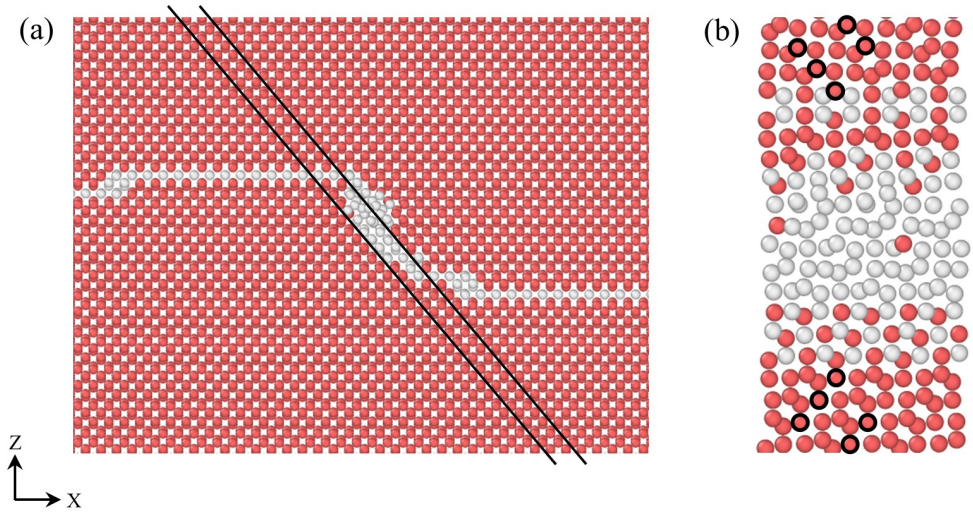


Figure 5. (a) Twin boundary facet in the $[1\bar{2}10]$ direction, which shows a disconnection step near the bottom of the basin. (b) Two dimensional slice of the facet identifying the pyramidal-pyramidal interface with symmetric twist misorientation. Atoms are colored by Common Neighbor Analysis.

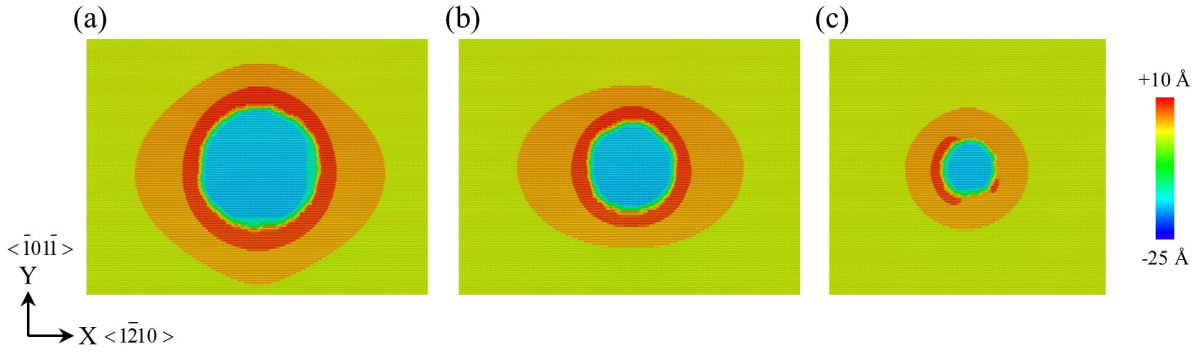


Figure 6. Influence of initial dislocation loop radius on the twin boundary defect structure. Initial radii of (a) 20 nm, (b) 15 nm and (c) 10 nm are employed. Atoms are colored by their Z coordinate position. The same field of view is used in each image; thus, the extremity of each image does not correspond to the boundaries of the simulation cell.

Figure 6 shows the effect of the initial dislocation loop radius on the final structure of the crater in the $\{10\bar{1}2\}$ twin boundary. The same field of view (zoom) is used in each of the images in Fig. 6 so that the relative size and shape of the islands and disconnection loops can be compared

meaningfully. The crater depth of 2.47 nm (25 $\{10\bar{1}2\}$ atomic planes inclusive of the rim) is consistent for all three cases. In general, similar structures are observed, including prominent PB interface facets at the ends of the island in the $< 10\bar{1}1 >$ directions. Each PB facet contains a misfit dislocation, similar to that shown in Figs. 3 and 4. There are, however, noticeable differences in the disconnection loops for the smallest crater. For the 20 nm and 15 nm radius craters, a double disconnection loop surrounds the entire crater. The interior loop has an average width of 5.0 nm in the 20 nm dislocation loop model and 4.0 nm in the 15 nm dislocation model. The outer loop is slightly elliptical with major axis in the $< 1\bar{2}10 >$ direction (direction of PP1 interfaces). However, for the 10 nm radius crater, the inner disconnection loop does not form completely, showing discontinuous atolls that are connected to the non-PB sections of the crater. The size-dependent structure of the defect is likely caused by the size-dependent stress state surrounding the crater, which influences the ability of the interior disconnection loop from completely forming around the smallest crater. For craters smaller than 10 nm, supplemental MD simulations show that a second disconnection ring does not appear.

**5. Kinetics of the Twin Boundary Defect**

In the atomistic simulations presented in Section 4, the sample was heated briefly to provide sufficient kinetic energy for the twin boundary defect to find a lower energy configuration than possible after the first energy minimization step. It is important to recall that the simulation cell is stress free. Thus, if discrete defects that comprise the crater on the $\{10\bar{1}2\}$ twin boundary are mobile, the crater should collapse during a lengthy annealing at $0.4T_{melt}$ if the kinetics are sufficiently fast to be captured within MD time scales.

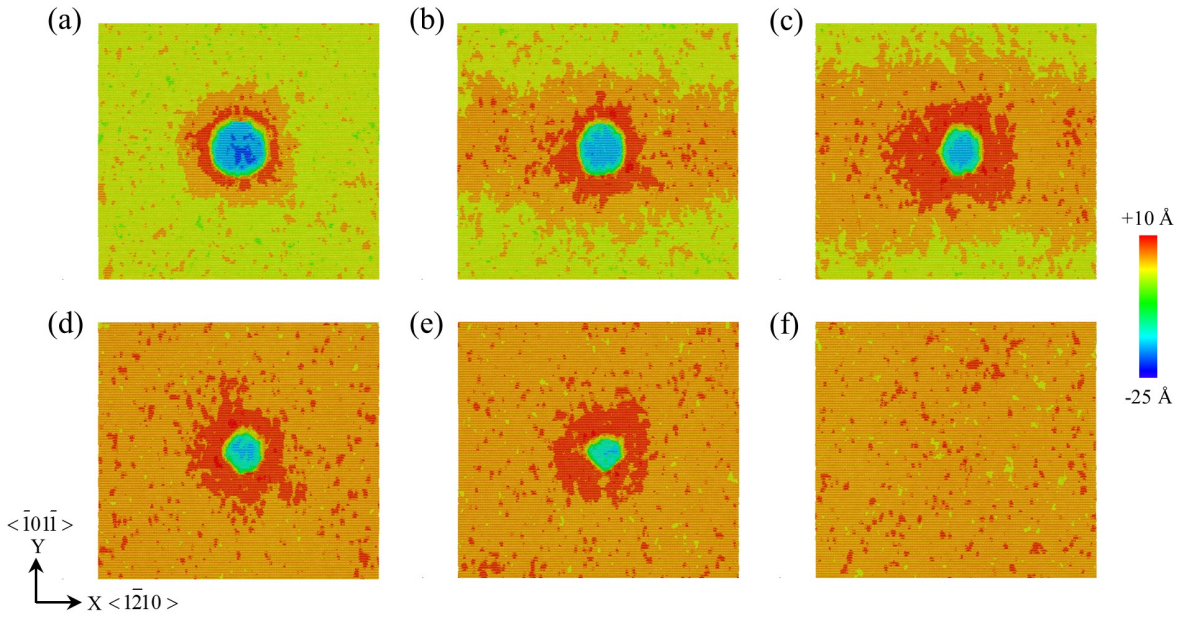


Figure 7. Time evolution of the 10 nm initial radius crater at $0.4T_{melt}$. The PB and PP1 boundaries of the crater are mobile under the self-stress field of the crater. The depth of the crater does not change appreciably until the final stages of the annihilation process. Atoms are colored by their Z coordinate position.

For example, for the smallest crater with initial radius 10 nm, Fig. 7 shows that the crater can shrink during a long annealing procedure implying that the boundaries that comprise the crater are mobile. Each image in Fig. 7 is created after a brief steepest decent procedure to eliminate thermal oscillations that would obscure the view. The disconnection loops on the exterior of the crater are highly mobile and take on extremely complex shapes, implying very low core energies. This observation is consistent for each of the crater sizes considered. In fact, the outermost disconnection ring is sufficiently mobile to combine with its image through the periodic boundary, raising the Z elevation of the $\{10\bar{1}2\}$ twin boundary. Conceivably, if the atomistic model was larger within the XY plane, this would not happen. The inner disconnection loop does not expand to react with its periodic image.

The PP1 and PB boundaries bounding the crater migrate at different rates, as the crater initially takes on a more elliptical shape during the annealing process; this is quantified in Fig. 8 for each dislocation loop radius considered. Initially, the PP1 interfaces move faster than the PB interfaces, as the separation distance between the PB boundaries of the crater is consistently greater than the separation distance between the PP1 boundaries. This causes the slightly elliptical shape of the crater as shown for the 10 nm initial radius crater in Fig. 7, the extent of which can be measured from Fig. 8. However, recall that the motion of an interface depends on both its mobility and the local driving force (stress state). As the shape of the crater evolves, the stress field of the crater evolves, and later in the annealing process, the PB interfaces begin to move faster, leading to an approximately circular crater immediately before annihilation, as shown in Fig. 8. The depth of the crater floor is consistent throughout most of the annealing process. The crater floor elevates to meet the Z position of the $\{10\bar{1}2\}$ boundary upon final annihilation. This process includes the motion of disconnections along the crater floor, which are responsible for changing the vertical position of the crater floor (Spearot et al., 2019).

As stated in the Introduction, the intersection between facets can be described by disclinations. The results shown here imply that the disclinations that comprise the boundaries of the crater can glide on the $\{10\bar{1}2\}$ plane without changing the depth of the crater. In addition, it is found that reduction in the depth of the crater requires climb of disclinations on the basal planes with elementary disconnection emission on the $\{10\bar{1}2\}$ plane. Using disclination dynamics this process has been shown to be energetically possible (Capolungo and Taupin, 2019).

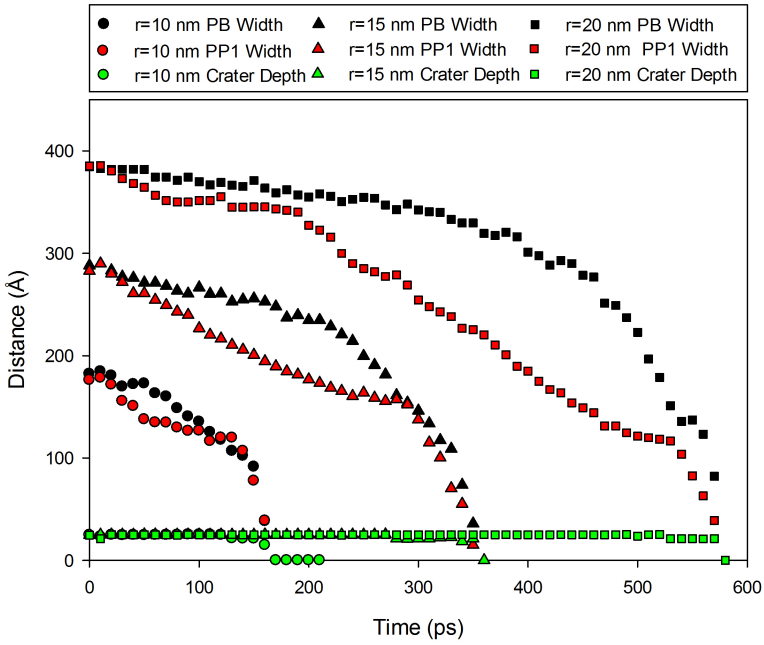


Figure 8. Time evolution of the separation distance between PB and PP1 boundaries and the depth of the crater floor during collapse of the crater under its self-stress field.

## 6. Anisotropic phase-field twin model

The MD simulations in Fig. 8 clearly show that the migration rate of facets depends on their orientation and structure. Here, a phase-field (PF) model is proposed to assess whether these differences are due to anisotropic facet mobility and energy, or simply due to the different stress/driving forces acting on the different facets (i.e., self-stress, capillary forces). To this end, four phase-field models are tested: (i) PF model 1 employs isotropic interface energies and mobilities, (ii) PF model 2 includes isotropic interface energies but with anisotropic mobilities, (iii) PF model 3 uses an anisotropic energy map containing energy values obtained from MD for equilibrium interfaces (CTB, PB, PP1 as thin, low energy interfaces) and anisotropic mobilities and (iv) PF model 4 employs anisotropic energies considering nonequilibrium interfaces (PB and PP1 are thick, defected high-energy interfaces) and anisotropic mobilities. PF model 1 is expected to reveal mostly the effect of stress and capillary forces. PF model 2 will show the

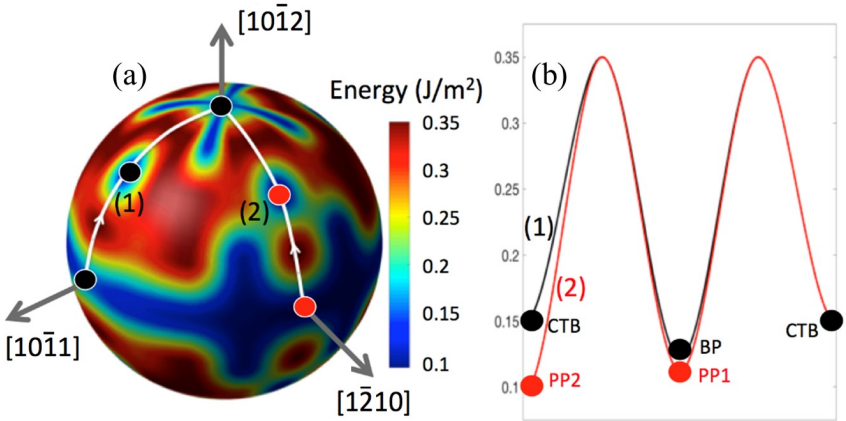


Figure 9. (a) Twin interface excess energy as a function of interface normal (J/m$^2$) mapped onto a spherical coordinate system. This map contains in particular MD values for equilibrium CTB, BP, PP1 and PP2 interfaces. (b) Energy profiles along the 2 white lines shown in (a).

effect of anisotropic mobility, while PF models 3 and 4 provide an assessment of the role of equilibrium or nonequilibrium interfaces and their associated energies on crater kinetics.

Specifically, PF model 1 assumes that all facets have energy equal to that of the CTB, taken as 0.13 J/m$^2$, and that all facets have the same mobility, L=$10^{-2}$ $(Pa \cdot s)^{-1}$. In PF model 2, simple anisotropy of interface mobility is introduced. All interfaces have the same mobility L=$10^{-2}$ $(Pa \cdot s)^{-1}$, except the CTB interface, which is specified with a mobility arbitrarily reduced by a factor 30. Of course, the mobility of interfaces should depend in a complex manner not only on the type of interfaces, but also on temperature, stress and activation energies specific to the mechanisms active during motion. MD simulations can be used to better define these values (Spearot et al., 2019). Incorporating this level of detail is beyond the scope of the current work.

In PF models 3 and 4, the lower mobility of CTB interfaces is retained and anisotropy of the interfacial energy is introduced. Specifically, in PF model 3, the energy map shown in Fig. 9 is introduced. Projecting the facet normal (the gradient of the phase-field) onto a spherical

coordinate system, one can introduce a continuous mapping of the anisotropic interface excess energy. Energy profiles in the spherical map from $[10\bar{1}1]$ to $[10\bar{1}2]$ (profile 1) and from $[1\bar{2}10]$ to $[10\bar{1}2]$ (profile 2) are introduced, using local minimum CTB energy, $\gamma = 0.149\, J/m^2$, PB energy, $\gamma = 0.122\, J/m^2$, PP1 energy, $\gamma = 0.112\, J/m^2$ and PP2 energy $\gamma = 0.1\, J/m^2$. For any facet normal in the spherical map, a bi-cubic Hermite spline interpolation is used to calculate the excess energy. Higher energies between the local minima introduced in the map are expected to penalize the formation of the associated facets, such that no facet other than the one specifically introduced is expected to form in the simulations. To date, there is no complete quantification of the excess energy of all possible facets. Further, in a realistic scenario, one must consider that each facet may adopt a different structure depending on defect content, resulting in significant complexity in the energy landscape. Importantly, the map used in PF model 3 and shown in Fig. 9 uses energies for equilibrium interfaces. However, MD simulation results show that PB and PP1 interfaces contain defects and therefore their thermodynamics may significantly differ from the equilibrium conditions assumed in PF model 3. Thus, in PF model 4, the energy of interfaces are chosen to best mimic the MD simulation results. Specifically, all interfaces will have the same energy $\gamma = 0.13\, J/m^2$, except those oriented at 45 degrees with respect to CTB planes for which $\gamma = 0.3\, J/m^2$ is used to model thicker high-energy nonequilibrium interfaces.

The phase-field model is now presented. Let the scalar phase-field variable $\phi$ represent the local twin volume fraction at a material point. With this, the matrix phase corresponds to $\phi = 0$ while the twin phase corresponds to $\phi = 1$. The spatial region where $0 < \phi < 1$ represents the twin boundary. Within this phase-field model, the Helmholtz free energy contains three contributions corresponding to the elastic strain energy of the system *E*, the barrier energy for the formation of

an interface *f* and the interfacial gradient energy Γ (Clayton and Knap, 2011; Heo et al., 2011; Kondo et al., 2014),

$$F = \iiint_V (E + f + \Gamma) dV \tag{4}$$

Here, $V$ represents the simulation domain. The elastic strain energy density is given by,

$$E = \frac{1}{2} \boldsymbol{\varepsilon^e} : \boldsymbol{C} : \boldsymbol{\varepsilon^e} \tag{5}$$

where both local elastic strain $\boldsymbol{\varepsilon^e}$ and stiffness tensor $\boldsymbol{C}$ depend on the phase-field variable $\phi$ (Clayton and Knap, 2011),

$$\boldsymbol{\varepsilon^e} = \boldsymbol{\varepsilon} - h(\phi)\boldsymbol{\varepsilon^{tw}} \tag{6}$$

$$\boldsymbol{C} = \big(1 - h(\phi)\big)\boldsymbol{C^M} + h(\phi)\, \boldsymbol{C^{tw}} \tag{7}$$

The constant stiffness tensors of the matrix and twin phases are denoted with $\boldsymbol{C^M}$ and $\boldsymbol{C^{tw}}$. The phase-field interpolation function is chosen as $h(\phi) = \phi^2(3 - 2\phi)$ with derivative $h'(\phi) = \frac{\partial h}{\partial \phi} = 6(\phi - \phi^2)$. The tensor $\boldsymbol{\varepsilon}$ denotes the total strain tensor, while the tensor $\boldsymbol{\varepsilon^{tw}}$ describes the eigenstrain resulting from the twinning transformation, with components $\varepsilon_{13}^{tw} = \varepsilon_{31}^{tw} = s/2$ and *s* being the twinning shear. Thus, to calculate the Cauchy stress tensor, $\boldsymbol{\sigma}$, in the phase-field simulation,

$$\boldsymbol{\sigma} = \frac{\partial E}{\partial \boldsymbol{\varepsilon^e}} = \boldsymbol{C}: \boldsymbol{\varepsilon^e} = \big(1 - h(\phi)\big)\boldsymbol{C^M}: (\boldsymbol{\varepsilon} - h(\phi)\boldsymbol{\varepsilon^{tw}}) + h(\phi)\, \boldsymbol{C^{tw}}: (\boldsymbol{\varepsilon} - h(\phi)\boldsymbol{\varepsilon^{tw}}) \quad (8)$$

The barrier energy *f* takes the following double-well potential form (cf. (Allen and Cahn, 1979; Boettinger et al., 2002; Chen, 2002; Steinbach, 2009; Thornton et al., 2003)),

$$f(\phi) = W\, \phi^2(1-\phi)^2 \quad (9)$$

where $W$ is the height of the energy barrier. The arbitrary value $W$=7.5 $10^8$ J/m$^3$ is selected. The derivative of the barrier energy with respect to $\phi$ is $f'(\phi) = \frac{\partial f}{\partial \phi} = 2W\big(\phi(1-\phi)^2 - \phi^2(1-\phi)\big)$. More realistic shapes and heights for the energy barrier can be obtained from atomistic simulations (Gu et al., 2013). The interfacial gradient energy Γ reads,

$$\Gamma = \frac{1}{2}\boldsymbol{\kappa}(\boldsymbol{\nabla}\phi) : (\boldsymbol{\nabla}\phi \otimes \boldsymbol{\nabla}\phi) \quad (10)$$

where $\boldsymbol{\nabla}$ is the Nabla operator. The operator $\otimes$ denotes the dyadic product between two vectors. The matrix $\boldsymbol{\kappa}$ is a diagonal matrix. Following recent works (Eggleston et al., 2001), $\kappa_{11} = \kappa_{22} = \kappa_{33} = \kappa$ and includes dependence on $\boldsymbol{\nabla}\phi$ to introduce an orientation dependent interfacial energy. Specifically, the local value of $\boldsymbol{\nabla}\phi$ provides the direction of the local interface unit normal vector **n**. From Allen and Cahn (Allen and Cahn, 1979), the interface excess energy $\gamma$ is related to $\kappa$ and $W$ as $\gamma = \sqrt{\kappa W}/3$. The interface thickness $t$ is also a function of $\gamma$ and $W$ (Clayton and Knap,

2011), $t = 12\gamma/W$. For a fixed value of the barrier height, $W$, the thickness increases linearly with the interface excess energy.

The local spatiotemporal evolution of the phase-field variable follows the Allen-Cahn equation,

$$\frac{d\phi}{dt} = -L\frac{\partial F}{\partial \phi} \tag{11}$$

In Eq. (11), L is the mobility, which is anisotropic in PF models 2, 3 and 4. Similar to interfacial energy, a continuous map L($\boldsymbol{\nabla}\phi$) is defined. The derivative of the energy functional $F$ with respect to phase-field $\phi$ is,

$$\frac{\partial F}{\partial \phi} = \frac{\partial E}{\partial \phi} + \frac{\partial f}{\partial \phi} - \boldsymbol{\nabla} \cdot \frac{\partial \Gamma}{\partial \boldsymbol{\nabla}\phi} \tag{12}$$

The derivative of elastic energy density $E$ with respect to the phase-field variable $\phi$ reads (Clayton and Knap, 2011),

$$\frac{\partial E}{\partial \phi} = h'(\phi)\left(\frac{1}{2}\boldsymbol{\varepsilon^e}\colon(\boldsymbol{C^{tw}} - \boldsymbol{C^M})\colon\boldsymbol{\varepsilon^e} - \boldsymbol{\sigma}\colon\boldsymbol{\varepsilon^{tw}}\right) \tag{13}$$

Thus, using Eq. (13), the derivative of total energy with respect to the phase-field variable is,

$$\frac{\partial F}{\partial \phi} = h'(\phi)\left(\frac{1}{2}\boldsymbol{\varepsilon^e}\colon(\boldsymbol{C^{tw}} - \boldsymbol{C^M})\colon\boldsymbol{\varepsilon^e} - \boldsymbol{\sigma}\colon\boldsymbol{\varepsilon^{tw}}\right) + 2W\big(\phi(1-\phi)^2 - \phi^2(1-\phi)\big) - \boldsymbol{\nabla}\cdot \left(\kappa : \boldsymbol{M} + \frac{1}{2}\boldsymbol{T}\colon(\boldsymbol{\nabla}\phi \otimes \boldsymbol{\nabla}\phi)\right) \tag{14}$$

where tensors M and T can be expressed in their component form as follows:

$$M_{ijk} = \delta_{ik}\phi_{,j} \tag{15}$$

$$T_{ijk} = \frac{\partial \kappa_{ij}}{\partial(\nabla\phi)_k} \tag{16}$$

Here, $\delta_{ik}$ is the Kronecker delta. The first term on the right hand side of Eq. (14) is the driving force due to stress. The second term is the driving force due to barrier energy, which tends to compress facets (sharp phase-field gradients). The last term is the driving force due to anisotropic interface gradient energy, which tends to spread facets (diffuse phase-field gradients) depending on their excess energy.

The following moduli for Mg in the local crystal frame are employed $C_{11}$=$C_{22}$=59740 MPa, $C_{33}$=61700 MPa, $C_{12}$=26240 MPa, $C_{13}$=$C_{23}$=21700 MPa and $C_{44}$=$C_{55}$=$C_{66}$=34883 MPa. These moduli are used to compute tensors $\boldsymbol{C^M}$ and $\boldsymbol{C^{tw}}$ in the global coordinate system. The phase-field equations are numerically approximated with a spectral code using Fast Fourier Transform (FFT) algorithms. At each time step, for a given distribution of the phase-field, the balance of Cauchy stress field, Eq. (8), is solved by using the accelerated scheme (Michel et al., 2001). Importantly, the computation of spatial derivatives in Fourier space can lead to Gibbs fluctuations. To mitigate this, the modified Green tensor is computed with use of discrete Fourier transform operators following the rotated scheme proposed by Willot (Willot, 2015). In addition, any other spatial derivatives appearing on the right hand side of Eq. (12) are computed via the use of 1$^{st}$ and 2$^{nd}$ order centered finite difference schemes (table provided in (Berbenni et al., 2016)).

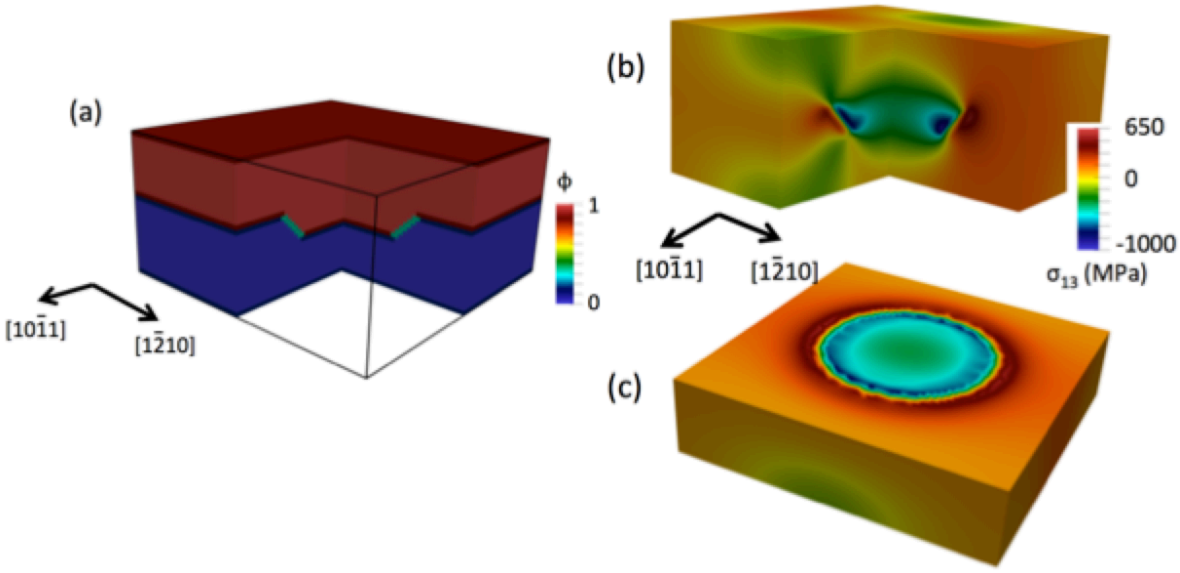


Figure 10. Initial construction of a crater in the phase-field model. (a) Phase-field distribution, the twin phase corresponds to φ=1. (b) View of the internal shear stress field on planes perpendicular to twinning shear and transverse directions. (c) View of the internal shear stress field on a plane perpendicular to twinning normal direction. The overall shear stress of -1.2GPa induced by the twin phase has been subtracted.

The initial structure of the crater is shown in Fig. 10(a). A crater similar to that shown in Fig. 6(c) is created by adding a supplementary conic twin phase domain that penetrates the lower matrix region. The mean crater radius is 10 nm and its depth is 3 nm, approximately matching the equilibrated geometry reported by MD simulations. The initial interfaces composing the crater are set at an angle of 45° with respect to the initial CTB. The two disconnection rings surrounding the crater in the Fig. 6 are neglected.

The FFT grid is composed of 64*64*32 voxels in the twinning shear, transverse and normal directions, respectively. The size of the grid is sufficient for the present study. The voxel resolution is 0.5 nm in all directions. It is confirmed that the interfaces with low energy are sufficiently diffuse and can move under low applied stresses (i.e., no numerical pinning occurs). Importantly, in phase-field simulations, a macroscopic stress is imposed on the volume to nullify

the average stress induced by the twin phase in the domain (-1.2 GPa). This is required since the internal stress due to the twin transformation is not explicitly introduced to create the crater in the atomistic simulations. It is confirmed that this value remains nearly constant during the annihilation simulations. The resulting internal shear stress due to the crater is shown in Figs. 10(b) and 10(c).

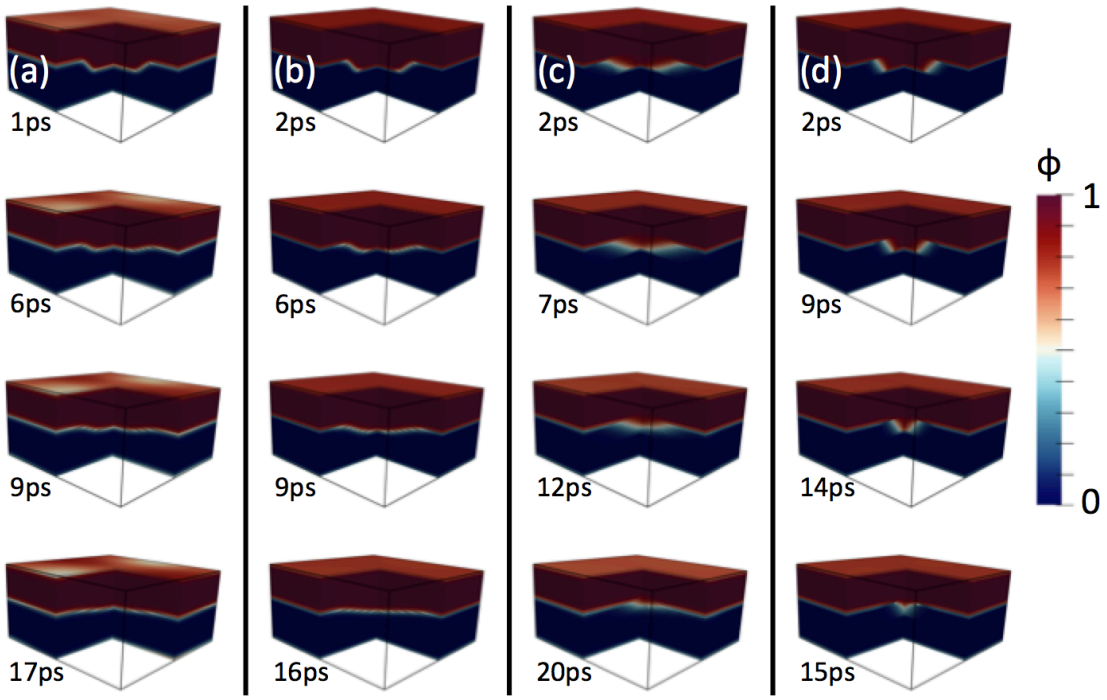


Figure 11. Evolution of the crater during self-relaxation. The view orientation is the same as in Fig. 10(b). Images are colored by the phase-field variable, interfaces appear in white with the color scheme chosen. Columns (a, b, c and d) show the predictions by each phase-field model (1, 2, 3 and 4).

Figures 11 and 12 show the evolution of the crater predicted by the four PF models, with the time evolution of the crater depth shown in Fig. 13, compared with atomistic simulation results. All four simulations predict the collapse of the crater, but with different kinematics and kinetics.

PF model 1 is in significant disagreement with atomistic simulations. Figures 11(a) and 12(a) show that the annihilation process is mostly controlled by "capillary" forces, such that the crater interfaces quickly flatten and the crater floor rapidly moves upwards towards the CTB. However, MD simulations show that the crater floor does not elevate during the annihilation sequence until the final stages; rather, annihilation is controlled by the mobility of crater interfaces, including the PB and PP1 facets, which should move relatively uniformly so as to preserve the angle between the crater floor and its sides. In the PF model 1 simulation, however, the initial angle of 45 degrees quickly decreases leading to an incorrect evolution of the crater depth with time, as reported in Fig. 13.

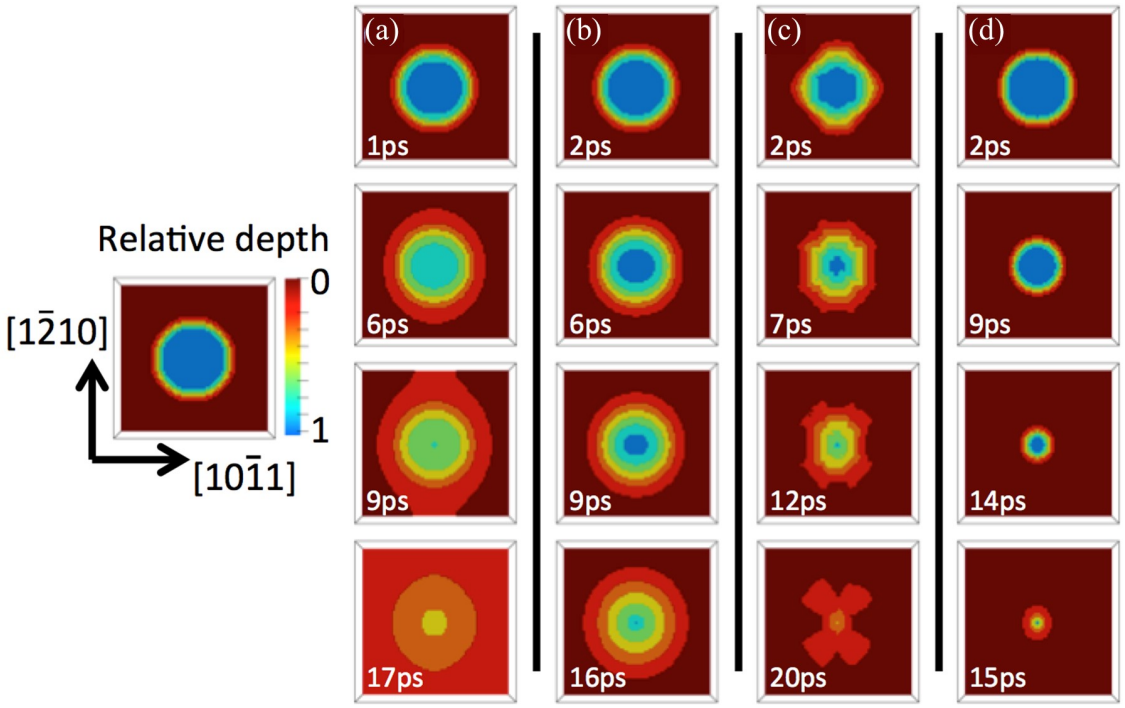


Figure 12. Top view of the evolution of the crater during self-relaxation. The initial crater geometry is shown on the left, where color shows the relative depth of the crater (red is the top, blue is the crater floor). Columns (a, b, c and d) show the predictions provided by each phase-field model (1, 2, 3 and 4).

To assess first whether anisotropic mobility is required to capture the kinematics of the crater relaxation process, PF model 2 arbitrarily reduces the mobility of the CTB interface by a factor of 30, but maintains isotropic facet energies. The simulation result with PF model 2 is now in better agreement with MD simulation results in that the annihilation is controlled by the mobility of facets that connect the top and bottom of the crater. However, these interfaces do not preserve the angle between the top and bottom of the crater during motion, as shown in Fig. 11(b).

Next, to evaluate the importance of facet orientation dependent interface energy, PF models 3 and 4 consider a more complex energy landscape. In PF model 3, the energy map shown in Fig. 9 is employed. Note, all interfaces are considered to be fully-coherent and defect free, in contrast with the MD predictions. Figures 11-13 show that these simulation results are in better agreement with the MD predictions; however, the angle between the crater floor and the CTB is still not maintained during the annihilation sequence, and diffuse interfaces are observed. Thus, in PF model 4, to consider defect-containing interfaces, albeit in an approximate fashion, all interfaces are posed with the same energy $\gamma = 0.13\, J/m^2$, except those oriented at 45° with respect to CTB planes for which a higher value $\gamma = 0.3\, J/m^2$ is chosen. The simulation result provides the closest agreement with the MD predictions, as shown in Figs. 11-13. The non-CTB interfaces now move uniformly and are thicker than the CTB facets. The depth of the crater is maintained until the final stages of the annihilation process, which is in much better agreement with the atomistic simulation results. Ultimately, this demonstrates that the behavior of nonequilibrium states of common interfaces must be considered to properly capture kinetics and kinematics associated with twin transformations in Mg.

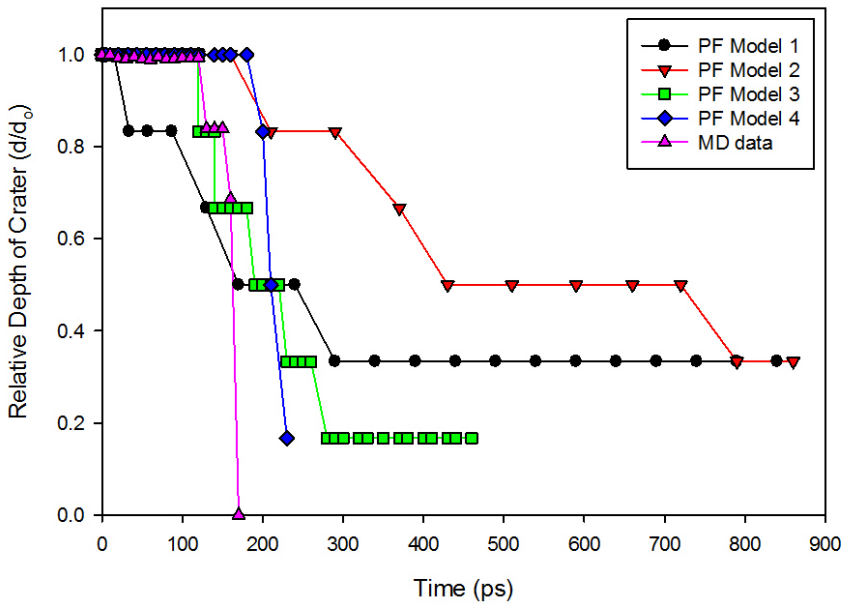


Figure 13. Evolution of the relative crater depth with time, as predicted from the different phase-field models tested, with comparison with the MD simulation result.

## 7. Conclusions

In this study, MD simulations are used to characterize the structure of nonequilibrium facets that separate $\{10\bar{1}2\}$ twin domains from their host grain in pure Mg. Furthermore, the intent of this work is to study the three dimensional nature of twin domains. To this end, a new technique is proposed to create a crater on the $\{10\bar{1}2\}$ twin boundary. Simulations reveal that the crater is composed of facets including those with PB and PP1 orientations. However, a close examination of these facets shows that they can contain additional defects to accommodate the misfit across the twin boundary. The radius of the crater does not influence the depth of the crater, but the radius of the crater (and thus its stress field) does influence the conformation of disconnection rings that surround the crater. When heated, MD simulations reveal that the migration rate of facets depends on their orientation/structure. An anisotropic phase-field model is proposed to assess whether these differences are due to anisotropic facet mobility and/or energy, or simply due to the different stress and capillary driving forces acting on the different facets. Using an

isotropic PF model predicts the collapse of the crater assisted by its own backstress and strong capillary forces, but the kinematics and kinetics of facets are in significant disagreement with MD simulations. To ensure that inclined facets control the annihilation process it is found that the use of anisotropic mobilities are required. Specifically, simulations suggest that the intrinsic mobility of CTB interfaces must be significantly lower than that of crater inclined facets. Further, MD simulation results are best matched via the introduction of facet orientation dependent excess energies, which are designed to approximate the role of defects within the bounding interfaces. The crater employed in this work provides a construct that allows a deconvolution of the roles of energy and mobility for select interfaces. These results suggest that it is important to systematically explore additional nonequilibrium interface structures and behaviors.

**Acknowledgements**

This work was funded by the U.S. Dept. of Energy, Office of Basic Energy Sciences Project FWP 06SCPE401. DES acknowledges the University of Florida Research Computing for providing computational resources used for obtaining the research results reported in this publication. M. Gong is acknowledged for providing values of equilibrium interface energies. A. Ruffini and P.A. Geslin are acknowledged for helpful discussions on theoretical and numerical aspects related to phase-field modeling.

**Competing Interests**

The authors declare no competing interests.

**References**


Allen, S.M., Cahn, J.W., 1979. A microscopic theory for antiphase boundary motion and its application to antiphase domain coarsening. Acta Metall. 27, 1085–1095.

Barnett, D.M., 1985. The displacement field of a triangular dislocation loop. Philos. Mag. A 51, 383–387.

Barnett, D.M., Balluffi, R.W., 2007. The displacement field of a triangular dislocation loop–a correction with commentary. Philos. Mag. Lett. 87, 943–944. https://doi.org/10.1080/09500830701601748

Barrett, C.D., El Kadiri, H., 2014a. Impact of deformation faceting on {10-12}, {10-11} and {10-13} embryonic twin nucleation in hexagonal close-packed metals. Acta Mater. 70, 137–161. https://doi.org/10.1016/j.actamat.2014.02.018

Barrett, C.D., El Kadiri, H., 2014b. The roles of grain boundary dislocations and disclinations in the nucleation of {10-12} twinning. Acta Mater. 63, 1–15. https://doi.org/10.1016/j.actamat.2013.09.012

Berbenni, S., Taupin, V., Fressengeas, C., Capolungo, L., 2016. A Fast Fourier Transform-Based Approach for Generalized Disclination Mechanics Within a Couple Stress Theory, in: Altenbach, H., Forest, S. (Eds.), Generalized Continua as Models for Classical and Advanced Materials. Advanced Structured Materials. Springer.

Bitzek, E., Brandl, C., Weygand, D., Derlet, P.M., Van Swygenhoven, H., 2009. Atomistic simulation of a dislocation shear loop interacting with grain boundaries in nanocrystalline aluminium. Model. Simul. Mater. Sci. Eng. 17, 055008. https://doi.org/10.1088/0965-0393/17/5/055008

Boettinger, W.J., Warren, J.A., Beckermann, C., Karma, A., 2002. Phase-Field Simulation of Solidification. Annu. Rev. Mater. Res. 32, 163–194. https://doi.org/10.1146/annurev.matsci.32.101901.155803

Capolungo, L., Taupin, V., 2019. GD3: generalized discrete defect dynamics. Mater. Theory 3, 1–21. https://doi.org/10.1186/s41313-018-0013-9

Chen, L., 2002. Phase-Field Models for Microstructure Evolution. Annu. Rev. Mater. Res. 32, 113–140. https://doi.org/10.1146/annurev.matsci.32.112001.132041

Christian, J.W., Mahajan, S., 1995. Deformation twinning. Prog. Mater. Sci. 39, 1–157. https://doi.org/10.1016/0079-6425(94)00007-7

Clayton, J.D., Knap, J., 2011. A phase field model of deformation twinning: Nonlinear theory and numerical simulations. Phys. D Nonlinear Phenom. 240, 841–858. https://doi.org/10.1016/j.physd.2010.12.012

Dang, K., Bamney, D., Bootsita, K., Capolungo, L., Spearot, D.E.D.E., 2019. Mobility of dislocations in Aluminum: Faceting and asymmetry during nanoscale dislocation shear loop expansion. Acta Mater. 168, 426–435. https://doi.org/10.1016/j.actamat.2019.02.034

Dang, K., Capolungo, L., Spearot, D.E., 2017. Nanoscale dislocation shear loops at static equilibrium and finite temperature. Model. Simul. Mater. Sci. Eng. 25, 085014. https://doi.org/10.1088/1361-651X/aa9390

Eggleston, J.J., McFadden, G.B., Voorhees, P.W., 2001. A phase-field model for highly anisotropic interfacial energy. Phys. D Nonlinear Phenom. 150, 91–103. https://doi.org/10.1016/S0167-2789(00)00222-0

Gu, Y., Chen, L.-Q., Heo, T.W., Sandoval, L., Belak, J., 2013. Phase field model of deformation twinning in tantalum: Parameterization via molecular dynamics. Scr. Mater. 68, 451–454. https://doi.org/10.1016/j.scriptamat.2012.11.022

Hagege, S., Mori, M., Ishida, Y., 1990. Computer simulation of the (10(-1)2) twin atomic structure in HCP metals. J. Phys. Colloq. 51, 161–166.

Heo, T.W., Wang, Y., Bhattacharya, S., Sun, X., Hu, S., Chen, L.Q., 2011. A phase-field model for deformation twinning. Philos. Mag. Lett. 91, 110–121. https://doi.org/10.1080/09500839.2010.537284

Hirth, J.P., Pond, R.C., 1996. Steps, dislocations and disconnections as interface defects relating to structure and phase transformations. Acta Mater. 44, 4749–4763. https://doi.org/10.1016/S1359-6454(96)00132-2

Hirth, J.P., Pond, R.C., Lothe, J., 2006. Disconnections in tilt walls. Acta Mater. 54, 4237–4245. https://doi.org/10.1016/j.actamat.2006.05.017

Hirth, J.P., Wang, J., Tomé, C.N., 2016. Disconnections and other defects associated with twin interfaces. Prog. Mater. Sci. 83, 417–471. https://doi.org/10.1016/j.pmatsci.2016.07.003

Kim, Y., Kim, N.J., Lee, B., 2009. Atomistic Modeling of pure Mg and Mg–Al systems. CALPHAD Comput. Coupling Phase Diagrams Thermochem. 33, 650–657. https://doi.org/10.1016/j.calphad.2009.07.004

Kondo, R., Tadano, Y., Shizawa, K., 2014. A phase-field model of twinning and detwinning

coupled with dislocation-based crystal plasticity for HCP metals. Comput. Mater. Sci. 95, 672–683. https://doi.org/10.1016/j.commatsci.2014.08.034

Kumar, M.A., Clausen, B., Capolungo, L., McCabe, R.J., Liu, W., Tischler, J.Z., Tomé, C.N., 2018. Deformation twinning and grain partitioning in a hexagonal close-packed magnesium alloy. Nat. Commun. 9, 4761. https://doi.org/10.1038/s41467-018-07028-w

Kurtz, R.J., Hoagland, R.G., Hirth, J.P., 1999. Computer simulation of extrinsic grain-boundary defects in the ∑11, <101>{131} symmetric tilt boundary. Philos. Mag. A 79, 683–703. https://doi.org/10.1080/01418619908210325

Leclercq, L., Capolungo, L., Rodney, D., 2014. Atomic-Scale Comparison Between {-1101} and {-1102} Twin Growth Mechanisms in Magnesium. Mater. Res. Lett. 2, 152–159. https://doi.org/10.1080/21663831.2014.880548

Lentz, M., Risse, M., Schaefer, N., Reimers, W., Beyerlein, I.J., 2016. Strength and ductility with {10$\bar{1}$1} — {10$\bar{1}$2} double twinning in a magnesium alloy. Nat. Commun. 7, 11068. https://doi.org/10.1038/ncomms11068

Liu, B., Wang, J., Li, B., Lu, L., Zhang, X., Shan, Z., Li, J., Jia, C., Sun, J., Ma, E., 2014. Twinning-like lattice reorientation without a crystallographic twinning plane. Nat. Commun. 5, 3297, 1–5. https://doi.org/10.1038/ncomms4297

Liu, X.Y., Adams, J.B., Ercolessi, F., Moriarty, J.A., 1996. EAM potential for magnesium from quantum mechanical forces forces. Model. Simul. Mater. Sci. Eng. 4, 293–303.

Liu, Y., Li, N., Shao, S., Gong, M., Wang, J., McCabe, R.J., Jiang, Y., Tomé, C.N., 2016. Characterizing the boundary lateral to the shear direction of deformation twins in magnesium. Nat. Commun. 7, 11577. https://doi.org/10.1038/ncomms11577

Michel, J.C., Moulinec, H., Suquet, P., 2001. A computational scheme for linear and non-linear composites with arbitrary phase contrast. Int. J. Numer. Methods Eng. 52, 139–160. https://doi.org/10.1002/nme.275

Morris, J.R., Ye, Y., Yoo, M.H., 2005. First-principles examination of the (10-12) twin boundary in hcp metals. Philos. Mag. 85, 233–238. https://doi.org/10.1080/14786430412331315671

Ostapovets, A., Gröger, R., 2014. Twinning disconnections and basal–prismatic twin boundary in magnesium. Model. Simul. Mater. Sci. Eng. 22, 025015. https://doi.org/10.1088/0965-0393/22/2/025015

Ostapovets, A., Serra, A., 2014. Characterization of the matrix–twin interface of a (10-12) twin

during growth. Philos. Mag. 94, 2827–2839. https://doi.org/10.1080/14786435.2014.933906

Pei, Z., Sheng, H., Zhang, X., Li, R., Svendsen, B., 2018. Tunable twin stability and an accurate magnesium interatomic potential for dislocation-twin interactions. Mater. Des. 153, 232–241. https://doi.org/10.1016/j.matdes.2018.04.085

Pei, Z., Zhang, X., Hickel, T., Friák, M., Sandlöbes, S., Dutta, B., Neugebauer, J., 2017. Atomic structures of twin boundaries in hexagonal close-packed metallic crystals with particular focus on Mg. npj Comput. Mater. 6, 1–7. https://doi.org/10.1038/s41524-017-0010-6

Plimpton, S., 1995. Fast parallel algorithms for short-range molecular dynamics, Journal of Computational Physics. https://doi.org/10.1006/jcph.1995.1039

Rittner, J.D., Seidman, D.N., 1996. <110> symmetric tilt grain-boundary structures in fcc metals with low stacking-fault energies. Phys. Rev. B 54, 6999–7015. https://doi.org/10.1103/PhysRevB.54.6999

Shewchuk, J.R., 1994. An introduction to the conjugate gradient method without the agonizing pain. https://doi.org/10.1.1.110.418

Spearot, D.E., Capolungo, L., Tomé, C.N., 2019. Shear-driven motion of Mg {10-12} twin boundaries via disconnection terrace nucleation, growth, and coalescence. Phys. Rev. Mater. 3, 053606. https://doi.org/10.1103/physrevmaterials.3.053606

Spearot, D.E., McDowell, D.L., 2009. Atomistic modeling of grain boundaries and dislocation processes in metallic polycrystalline materials. J. Eng. Mater. Technol. 131, 041204. https://doi.org/10.1115/1.3183776

Steinbach, I., 2009. Phase-field models in materials science. Model. Simul. Mater. Sci. Eng. 17, 073001. https://doi.org/10.1088/0965-0393/17/7/073001

Sun, D.Y., Mendelev, M.I., Becker, C.A., Kudin, K., Haxhimali, T., Asta, M., Hoyt, J.J., 2006. Crystal-melt interfacial free energies in hcp metals: A molecular dynamics study of Mg. Phys. Rev. B 73, 024116. https://doi.org/10.1103/PhysRevB.73.024116

Thornton, K., Ågren, J., Voorhees, P.W., 2003. Modelling the evolution of phase boundaries in solids at the meso- and nano-scales. Acta Mater. 51, 5675–5710. https://doi.org/10.1016/j.actamat.2003.08.008

Wang, J., Hirth, J.P., Tomé, C.N., 2009a. (-1012) Twinning nucleation mechanisms in hexagonal-close-packed crystals. Acta Mater. 57, 5521–5530. https://doi.org/10.1016/j.actamat.2009.07.047

Wang, J., Hoagland, R.G., Hirth, J.P., Capolungo, L., Beyerlein, I.J., Tome, C.N., 2009b. Nucleation of a (-1012) twin in hexagonal close-packed crystals. Scr. Mater. 61, 903–906. https://doi.org/10.1016/j.scriptamat.2009.07.028

Wang, J., Yadav, S.K., Hirth, J.P., Tomé, C.N., Beyerlein, I.J., 2013. Pure-shuffle nucleation of deformation twins in hexagonal-close-packed metals. Mater. Res. Lett. 1, 126–132.

Wang, J., Yu, Q., Jiang, Y., Beyerlein, I.J., 2014. Twinning-associated boundaries in hexagonal close-packed metals. JOM 66, 95–101. https://doi.org/10.1007/s11837-013-0803-0

Wang, Y., Chen, L.-Q., Liu, Z.-K., Mathaudhu, S.N., 2010. First-principles calculations of twin-boundary and stacking-fault energies in magnesium. Scr. Mater. 62, 646–649. https://doi.org/10.1016/j.scriptamat.2010.01.014

Willot, F., 2015. Fourier-based schemes for computing the mechanical response of composites with accurate local fields. Comptes Rendus Mécanique 343, 232–245. https://doi.org/10.1016/j.crme.2014.12.005

Wu, Z., Francis, M.F.F., Curtin, W.A.A., 2015. Magnesium interatomic potential for simulating plasticity and fracture phenomena. Model. Simul. Mater. Sci. Eng. 23, 015004. https://doi.org/10.1088/0965-0393/23/1/015004

Xu, B., Capolungo, L., Rodney, D., 2013. On the importance of prismatic/basal interfaces in the growth of (-1012) twins in hexagonal close packed crystals. Scr. Mater. 68, 901–904. https://doi.org/10.1016/j.scriptamat.2013.02.023

Zu, Q., Tang, X., Xu, S., Guo, Y., 2017. Atomistic study of nucleation and migration of the basal/prismatic interfaces in Mg single crystals. Acta Mater. 130, 310–318. https://doi.org/10.1016/j.actamat.2017.03.035